Tunable Phase Transition via Radiative Loss Controlling in a Terahertz Attenuated Total Reflection-Based Metasurface

Lin Chen, *Member, IEEE*, Yifan Ge, Xiaofei Zang, Jingya Xie, Li Ding, Alexei V. Balakin, Alexander P. Shkurinov, and Yiming Zhu

***Abstract*—Actively controlling the phase of terahertz wave has received much attention. Here, we present a complete theoretical treatment by using coupled-mode theory to actively control the reflective wave phase in a attenuated total reflection-based metasurface. Controlling is achieved by variations in the air gap, enabling the radiative loss (radiative Q factor) to be continuously adjusted over a narrowband frequency range. A singularity can be found in the phase slope spectrum when the radiation loss is equal to the intrinsic loss determined by material properties. The theoretical results have been verified by simulation and the experimental results. The physical mechanism of this phase transition in attenuated total reflection configuration would pave the way for potential applications such as polarization modulation, and guide further research works for terahertz physics.**

***Index Terms*—Attenuated total reflection (ATR), coupled-mode theory (CMT), phase transition, spoof surface plasmons, terahertz (THz).**

Manuscript received May 14, 2019; revised July 20, 2019 and August 5, 2019; accepted August 20, 2019. Date of publication August 26, 2019; date of current version November 4, 2019. This work was supported in part by the National Key R&D Program of China under Grant 2018YFF01013003, in part by the Program of Shanghai Pujiang Program, China, under Grant 17PJD028, in part by the National Natural Science Foundation of China under Grant 61671302, Grant 61601291, and Grant 61722111, in part by the Shuguang Program supported by Shanghai Education Development Foundation and Shanghai Municipal Education Commission, China, under Grant 18SG44, in part by the 111 Project (D18014), in part by the International Joint Lab Program supported by Science and Technology Commission Shanghai Municipality under Grant 17590750300, and in part by the Ministry of Science and Higher Education within the State assignment FSRC «Crystallography and Photonics» RAS. *(Corresponding authors: Lin Chen; Yiming Zhu.)*

L. Chen is with the Shanghai Key Lab of Modern Optical System, University of Shanghai for Science and Technology, Shanghai 200093, China, and also with the Shanghai Institute of Intelligent Science and Technology, Tongji University, Shanghai 200092, China (e-mail: linchen@usst.edu.cn).

Y. Ge, X. Zang, J. Xie, L. Ding, and Y. Zhu are with the Shanghai Key Lab of Modern Optical System, University of Shanghai for Science and Technology, Shanghai 200093, China (e-mail: 1191226857@qq.com; xfzang@usst.edu.cn; xiejingya.ok@163.com; sunnylding@usst.edu.cn; ymzhu@usst.edu.cn).

A. V. Balakin and A. P. Shkurinov are with the Shanghai Key Lab of Modern Optical System, University of Shanghai for Science and Technology, Shanghai 200093, China, with the Faculty of Physics and International Laser Center, Lomonosov Moscow State University and ILIT RAS–Branch of the FSRC «Crystallography and Photonics» RAS, Moscow 19991, Russia (e-mail: a.v.balakin@physics.msu.ru; ashkurinov@physics.msu.ru).

Color versions of one or more of the figures in this article are available online at http://ieeexplore.ieee.org.

Digital Object Identifier 10.1109/TTHZ.2019.2937504

I. Introduction

THE requirement for terahertz (THz) devices is remarkably increasing owing to their applications in diversified areas [1]–[3]. Among THz devices, the ability of phase transition has been extremely vital due to the fact that they can open up new perspectives and applications in THz holograms, polarization converters, and beam deflectors [4]–[12]. Recently, the study of phase transition has been extended to passive systems achieved by using metasurfaces [13]–[20]. For instance, the phase transition systems based on a periodic grating can be modeled as two-port resonators and could be tuned electrically or optically in the THz range. This phase transition system supports resonant and Rayleigh–Wood anomalies and operates in the transmission type. Moreover, the related investigations have been done to study the phase diagram of a metal–insulator–metal (MIM) metasurface, which is simply governed by the intrinsic and radiative Q factors [18]–[20]. The critical transition can also be achieved for transmitted beams in chiral metamaterial, which is related to the intrinsic and radiative losses, similar to the phase change of the reflected beam in MIM structure [21].

In addition to the phase transition in MIM cavity, the phase transition was also observed in Brewster angle design [22] or attenuated total reflection (ATR) configuration [23]–[25] with prism coupling spoof surface plasmons polaritons (SPPs) configurations in THz range. We note that early contributions on periodic structures supporting complex surface modes in the microwave community can be traced back to the 1950s [26]–[29]. The surface waves confined on a corrugated surface in the perfect electric conductor (PEC) limit are somewhat called spoof SPPs because their properties are similar to those of SPPs in the visible region [30]–[32]. It can be seen that the resonance dip was found in the reflection spectrum due to excitation of spoof SPPs modes. The phase shift changes drastically at the critical point which gives maximum absorbance/minimum reflectivity, similar to phenomenon in MIM metasurface configuration [18]–[20], [33]. However, the clear and complete physical insight of the phase transition in prism coupling spoof SPPs configurations is ignored because a one-port single-mode resonator model which is suitable in MIM metasurfaces cannot be utilized to prism coupling spoof SPPs configurations [25], [34], [35]. Such phase transition in spoof SPPs configurations with coupling prism

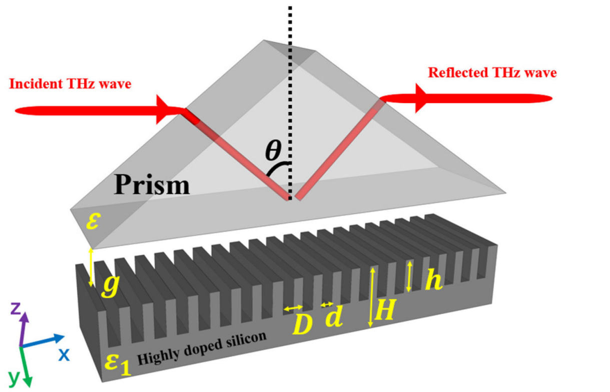

Fig. 1. Prism coupling spoof SPPs configuration with the period of the periodic grooves ($D = 60\ \mu$m), the width ($d = 30\ \mu$m), the groove height ($h = 60\ \mu$m), and the total height ($H = 120\ \mu$m). The air gap g can be tuned mechanically. A TM polarized beam is coupled to the spoof SPPs wave propagating in the $\hat{x}$ direction.

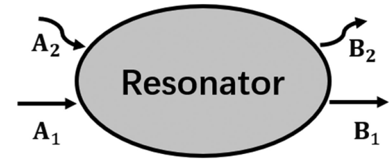

Fig. 2. Model of the two-port resonator described by CMT.

have potential applications in THz phase manipulations and polarization controls.

In this article, the phase transition in THz ATR configurations has been investigated by tailoring the radiative loss. A coupled-mode theory (CMT) model involving scattering parameters of one cell of the structure is used to explain the transition of the configuration. Moreover, we control the phase of a prism coupling spoof SPPs system by tailoring the radiative loss which is dynamically adjusted by mechanically tuning the air gap. Such a prism coupling technique was tracked back from experiments on integrated optics in the 1970s [36], [37]. The reflection coefficient can be easily obtained by the characteristic matrix of the medium at optical frequencies. However, the reflection coefficient and relative parameters are obtained more complicatedly by CMT due to the complex corrugated doped silicon surface. We present a complete theoretical treatment at THz frequencies by CMT, which provides clean insight of physical mechanism. Experimental results show good agreement with CMT. Besides the application of sensing with liquids through the grooves [25], this phase transition in ATR-based metasurface will have other potential applications in a different set of THz wave manipulation such as multifunctional polarization converter and THz fingerprint detection sensor.

II. CMT Analysis

Fig. 1 shows the designed THz ATR configuration with prism coupling spoof SPPs configuration. A Teflon prism was placed on the top with dielectric constant ε and was used for the phase matching [38]. An array of periodic grooves was fabricated in the highly doped silicon with a dielectric constant ε_1 which can be calculated by the Drude model [39], [40]. This structured surface supports spoof SPPs mode because doped silicon shows metallic properties in the THz range. The air gap between the prism and designed silicon can be adjusted mechanically. THz wave with transverse magnetic (TM) polarization ($\hat{H}$ in the $\hat{y}$ direction) is incident on the prism/air interface with the angle θ. Spoof SPPs mode with the vector k is excited on the corrugated surface and propagates in the $\hat{x}$ direction. In the following, according to the prism shape, THz wave is incident on the prism/air interface at an angle of 74.28° subject to total internal reflection. The penetration depth of the evanescent waves for the incident polarization is 56.368 μm at 0.78 THz [41].

The coupling principle can be described by the two-port resonator model as shown in Fig. 2, which consist one period of the doped silicon grating and the prism. In Fig. 2, A_2 and B_2 represents the THz beam incident on and reflected from the interface between the prism and the air gap, respectively. A_1 and B_1 is the coupling surface wave coming from the previous unit and transmitting to the next unit.

According to the CMT, the schematic in Fig. 2 can be described as

$$\begin{pmatrix} B_1 \\ B_2 \end{pmatrix} = \begin{pmatrix} t & \gamma \\ \gamma & r \end{pmatrix} \begin{pmatrix} A_1 \\ A_2 \end{pmatrix} \tag{1}$$

where t is the transmission coefficient of the spoof SPPs wave, r is the reflection coefficient of the incident wave at the prism/air interface, and γ is the coupling coefficient without consideration of the material loss. According to the above definition, the relation between the reflection coefficient and the coupling coefficient can be expressed as the following formula by using the energy conservation law:

$$|r|^2 + |\gamma|^2 = 1. \tag{2}$$

and B_1 and A_1 satisfy the following relationship:

$$B_1 = e^{-j\phi} * A_1 \tag{3}$$

where ϕ is the phase change between two adjacent cells which can be written as $\phi = \omega/c * \sqrt{\varepsilon} * \sin(\theta) * D$, and ω represents the angular frequency. Bringing (3) into (1), we get

$$B_1 = \frac{\gamma}{1 - e^{j\phi} *} * A_2 \tag{4}$$

$$B_2 = \left(r + \frac{\gamma^2 * e^{j\phi}}{1 - e^{j\phi} * t} \right) A_2. \tag{5}$$

Assuming $A_1 = 1$, the radiation-induced quality factor Q_{rad} can be given by

$$Q_{\text{rad}} = \omega * \frac{W}{|B'_2|^2} \tag{6}$$

where B_2' is the reflected wave coupling only from A_1, and the stored energy W in a periodic cell can be written as

$$W = |A_1|^2 * T \tag{7}$$

where T is the energy transportation time from one cell to the next cell and can be expressed as

$$T = \frac{D}{v_g} \tag{8}$$

where $v_g = d\omega/dk$ is the group velocity of the spoof SPPs wave. Combining with (6)–(8), the absolute value of coupling coefficient can be simplified as

$$|\gamma| = \frac{B'_2}{A_1} = \sqrt{\frac{2*\pi*D}{v_g} * \frac{c}{\lambda}} * \frac{1}{\sqrt{Q_{\text{rad}}}} = \sqrt{\frac{f}{f'(\Phi)}} * \frac{1}{\sqrt{Q_{\text{rad}}}}. \tag{9}$$

Here, the phase change (Φ) of one periodic cell without material loss is equal to $k*D$, and $f'(\Phi) = df/d\Phi$, where $f(\Phi)$ can be derived by the accurate dispersion relation in one-dimensional (1-D) grating structure including first-order diffraction, similar to Eq. (21) in [42]

$$1 = i\frac{d}{D}\frac{\omega}{\text{c}}\tan\left(\frac{\omega h}{c}\right)\sum_{n=-1}^{+1}\frac{\text{sinc}^2(k_n d/2)}{\alpha_0(k_n)} \tag{10}$$

where $k_n = k + (2\pi n/D)$ and $\alpha_0(k_n) = [(\frac{\omega}{c})^2 - k_n^2]^{1/2}$, where k is the wave vector propagating in the corrugated grating.

According to (6), the radiation-induced Q factor without the material loss is

$$Q_{\text{rad}} = \frac{f}{f'(\Phi)} * \frac{1}{|\gamma|^2}. \tag{11}$$

Next, we obtain the material loss induced Q factor Q_{int} without prism when $A_1 = 1$. Similar to (6), the Q_{int} can be described as

$$Q_{\text{int}} = \omega * \frac{W}{1 - |B_1|^2}. \tag{12}$$

Owing to the loss of the periodic-doped silicon, the relation between the transmission coefficient and the coupling coefficient can also be obtained

$$|t|^2 + |\gamma|^2 + \frac{f}{f'(\Phi)} * \frac{1}{Q_{\text{int}}} = 1. \tag{13}$$

The absolute value of coupling parameters can be found by substituting (11) into (2) and (13)

$$|r| = \sqrt{1 - \frac{f}{f'(\Phi)} * \frac{1}{Q_{\text{rad}}}} \tag{14}$$

$$|t| = \sqrt{1 - \frac{f}{f'(\Phi)} * \left(\frac{1}{Q_{\text{rad}}} + \frac{1}{Q_{\text{int}}}\right)}. \tag{15}$$

Finally, we determine the phase of r, t, and γ. The phase of r can be approximated by the phase shift of a TM wave when it undergoes total internal reflection [41]

$$\varphi(r) = \frac{k_0\sqrt{\varepsilon}\cos\theta - \varepsilon k_0\sqrt{\varepsilon\sin^2\theta - 1}}{k_0\sqrt{\varepsilon}\cos\theta + \varepsilon k_0\sqrt{\varepsilon\sin^2\theta - 1}} \tag{16}$$

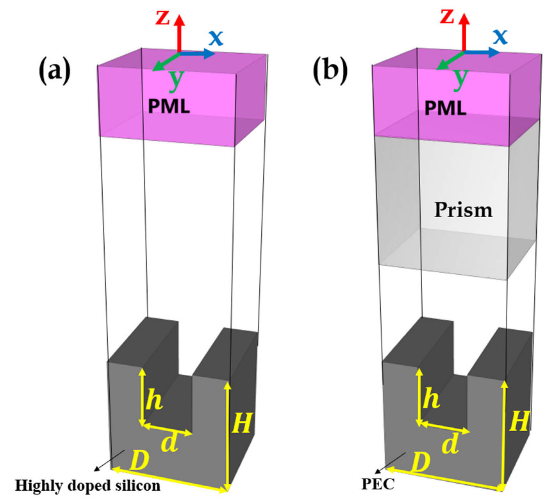

Fig. 3. (a) One cell of the periodic structure without prism but with a metallic loss for calculation of Ψ and Q_{int}. (b) One cell of the periodic structure without metallic loss but with prism for calculation of Φ and γ.

And the phase of t is equal to

$$\varphi(t) = -(\Phi + \Psi). \tag{17}$$

Here, Ψ is the additional phase caused by material loss. The phase of γ can be calculated as

$$2\varphi(\gamma) - \varphi(r) = \varphi(t) + \pi. \tag{18}$$

We note that the four key coupling parameters in CMT (Φ, γ, ψ, and Q_{int}) are obtained by using Ansoft HFSS. A method for extraction of Ψ and Q_{int} which are independent of the air gap can be used by eigenfrequency simulation of one period of the doped silicon grating with material loss but without prism as shown in Fig. 3(a). The boundaries should be set as master and slave boundaries (i.e., the periodic boundary). It is terminated vertically with a perfectly matched layer, which is located above the column to eliminate its effect on the field distribution. By setting the Floquet port, a plane wave is incident on periodic structure. Mesh and adaptive solutions (maximum number and maximum delta energy) are the default settings. We define the doped silicon grating by setting relative permittivity, bulk conductivity, and dielectric loss tangent [39], [40]. Meanwhile, we can also obtain the Φ and γ which are both the function of the air gap by performing the simulation of a cell with prism but without material loss [see Fig. 3(b)], where the grating is set as PEC. Periodic boundary condition is also used on sidewalls. Other conditions are similar to those in Fig. 3(a).

Equation (5) allows the reflected wave to be calculated for a given set of (Φ, γ, ψ, and Q_{int}). As described in the manuscript, ψ and Q_{int} represent the additional phase change which is caused by material loss and Q factor induced by the material loss, respectively. ψ and Q_{int} can be obtained from simulation of the period of the doped silicon without prism but with material loss, so these two parameters are independent of the air gap. Φ and γ represent the phase change through one periodic cell and the coupling coefficient, respectively. The two parameters can be calculated by simulating a cell with prism on the top

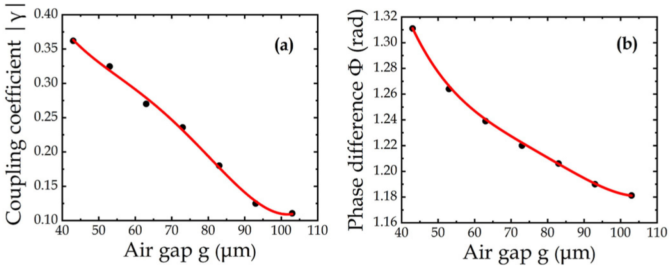

Fig. 4. (a) Coupling coefficient and (b) the phase difference through one periodic cell as a function of air gap g.

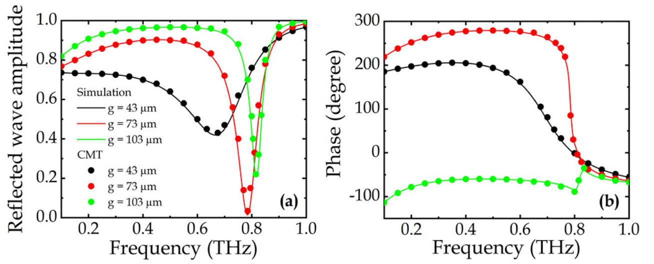

Fig. 5. (a) Amplitude and (b) phase of the reflected plane wave for air gap of 43, 73, and 103 μm. Solid curves are the results obtained from simulation and dots represent the results of CMT.

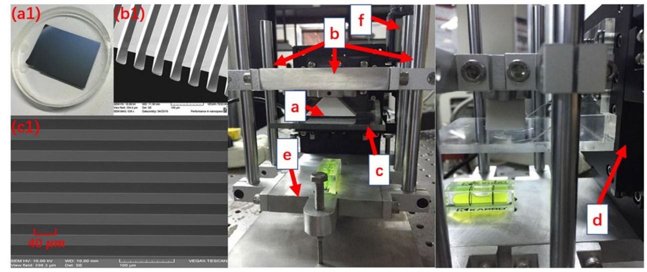

Fig. 6. Left: (a1) Photograph of the fabricated highly doped silicon with an array of periodic grooves, (b1) oblique view, and (c1) top view of SEM image. Right: Experimental ATR setup. (a) Coupling prism (Teflon), (b) the prism stand, (c) acrylic translation stage, (d) translation stage above the substrate (e), including a spiral micrometer and a liquid crystal display (f) that can show air gap in real time.

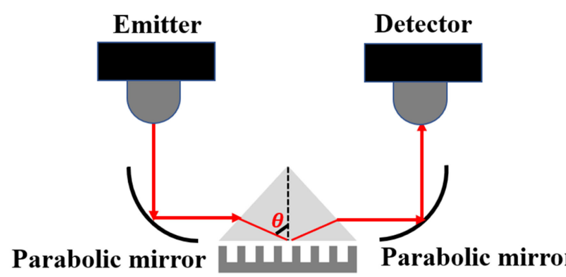

Fig. 7. Schematic illustration of the experimental setup.

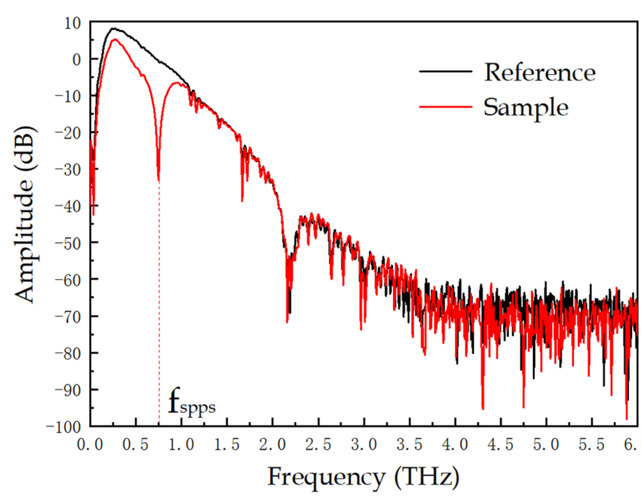

Fig. 8. Experimental spectrum of prism without doped silicon (reference) and with the corrugated doped silicon (sample). The air gap is 73 μm.

but without material loss, so they are the function of the air gap. Fig. 4(a) and (b) plots the dependence of two parameters on the air gap by using Ansoft HFSS. Fitted curves are also shown in Fig. 4(a) and (b). We can see that $|\gamma|$ decreases with increasing g due to the decreased radiative loss. Φ also decreases with increasing g. This is because the prism can disturb the spoof SPPs mode and modify its wave vector. Taking $g = 73$ μm, for example, we get $|\gamma| = 0.2358$ [see Fig. 4(a)], $\Phi = 1.22$ [see Fig. 4(b)], $\psi = 0.15$, and $Q_{\text{int}} = 172.13$. According to (13), (14), (16)–(18), the reflected wave amplitude and phase (solution to (5)) can be obtained as 0.0505° and 103.9°.

In order to demonstrate the validity of the CMT model, 2-D simulation has been carried out to obtain the reflectivity spectrum by using Ansoft HFSS with a single groove as the unit cell. Fig. 5(a) and (b) shows the reflected wave amplitude and phase with three air gaps, respectively. The results clearly show that minimum reflectivity (perfect absorption) occurs at the critical condition of the spoof plasmon frequency $f_c = 0.785$ THz and the air gap near 73 μm. Meanwhile, we could clearly observe the variable phase span across the resonance frequency from the underdamped ($g = 43$ μm) to the overdamped ($g = 103$ μm) regime with the increase of air gap.

III. Device Fabrication and Experimental Results

In the experiment, the array of periodic grooves was fabricated by using the traditional photolithography and the inductively coupled plasma etching on a doped silicon with resistivity of $1.07e - 3\,\Omega \cdot$ cm. Fig. 6(a1)–(c1) show the photograph and scanning electron microscope (SEM) images of the doped silicon with periodic grooves. The experimental ATR setup shown in Fig. 6(a)–(f) have been designed for coupling THz radiation into the spoof SPPs mode propagating on the periodic structure. The air gap can be easily tuned by adjusting a spiral micrometer on translation stage. The value of air gap displays in a small liquid crystal screen in real time.

The experiment was carried out via THz Time-Domain Spectroscopy (THz-TDS) for sample (prism with doped silicon grating) and reference (prism) and the humidity is 5% [38], [43]. A schematic illustration of the experimental setup is shown in Fig. 7. The spot size of the incident THz wave is 13 mm. The frequency spectrum was obtained from the time-domain signal by using the Fourier transform. Fig. 8 shows the measured frequency domain spectra of reference (black) E_{ref} and of the

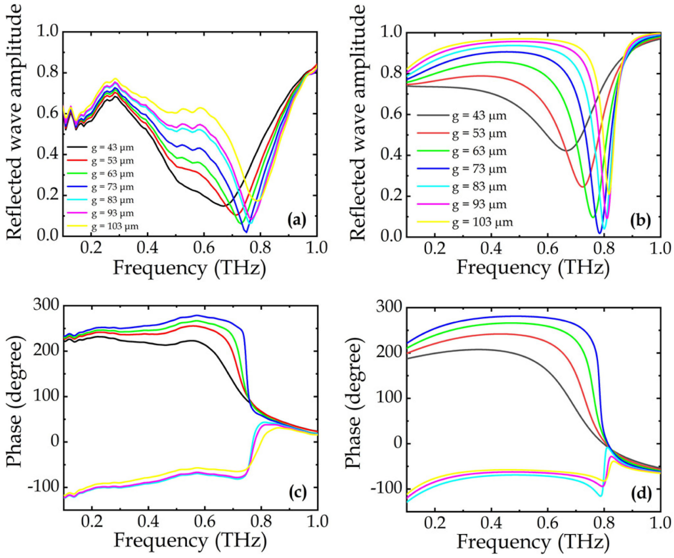

Fig. 9. (a) Reflected wave amplitude and (c) phase between reference signal and sample signal measured by THz-TDS. (b) and (d) Amplitude and phase of the reflected plane wave for different air gap obtained by CMT.

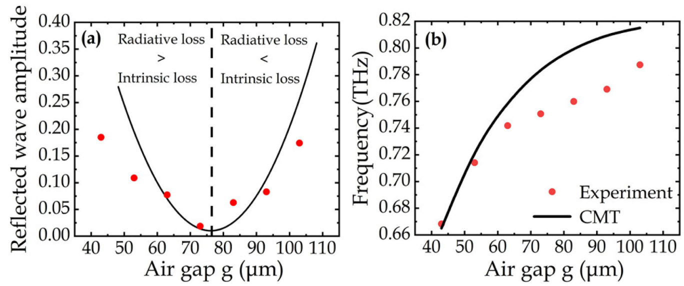

Fig. 10. (a) Reflected wave amplitude vs air gap. The experimental dots and theoretical curve are selected at the minimum reflectivity for different air gaps. (b) Resonance frequency with respect to air gap according to Fig. 9(a) and (b).

sample (red) $E_{\rm sam}$. The reflection with amplitude and phase information is normalized to the reference signals. As spoof SPPs mode is excited, a sharp dip at resonance frequency $f_{\rm spps}$ of 0.755 THz could be observed (red line). The additional resonance at 1.7 THz comes from the absorption of water vapor. And the resonance at 2.1 THz results from the prism. The reasons may come from the tiny nonuniform density in the Teflon prism.

The measured amplitude and phase spectra of the ATR configuration with different air gap are presented in Fig. 9(a) and (c). The calculated results by CMT are also shown in Fig. 9(b) and (d) for comparison. As predicted by the CMT, the inequality between the two quality factors would induce the phase transition. As we can see from Fig. 9(a) and (b), for $g = 43$ μm (at underdamped region), $Q_{\rm rad}$ is calculated as 62.45 by CMT, which is lower than the $Q_{\rm int}$, the phase changes in Fig. 9(c) and (d) show underdamping state, and the phase slope is negative value. When the air gap is near the critical condition ($g = 73$ μm), $Q_{\rm rad}$ is calculated as 170.06 by CMT, which is approximately equal to $Q_{\rm int}$ (172.13), the reflected wave amplitude exhibits perfect absorption shown in Fig. 9(a) and (b), the phase slope diverges to infinite negative value in the underdamped region. As *g* further increases, the radiative loss is decreased to less than the intrinsic loss. For $g = 103$ μm (at overdamped region), $Q_{\rm rad}$ is calculated as 813.99 by CMT, which is higher than the $Q_{\rm int}$, the phase changes in Fig. 9(c) and (d) show overdamping state, and the phase slope is positive value. The large phase span nearly 360° are observed in underdamped regime ($Q_{\rm rad} - Q_{\rm int} < 0$) and the phase span small range (<180°) in an overdamped regime ($Q_{\rm rad} - Q_{\rm int} > 0$). The phase slope indicates the phase jump effect by changing the air gap. Different from spacer thickness of the resonator that determines the Q factors [16], [20], the air gap in ATR configuration reveals a key impact on the radiative quality factor. Tailoring the air gap *g* provides a simple pathway to tune the difference between the quality factors. In addition, the Q factor of different resonances in Fig. 9(a) and (b) is determined by total loss (radiative and intrinsic losses) in system. As we know the radiative loss decreases with increasing gap while the intrinsic loss maintains constant, so the total loss is decreased, resulting in the increase of Q factor. As a result, we have experimentally demonstrated the active phase transition of the ATR-based metasurface between underdamped and overdamped regimes by manipulating the radiative loss.

Fig. 10(a) depicts how the air gap (or radiative loss) influence the perfect coupling. It is known that the absorbance decreases significantly if any of these two quality factors deviate from the equality condition [21]. When we tune the radiative loss, there is an optimum solution to air gap (g) by which $Q_{\rm rad} = Q_{\rm int}$ (perfect absorption occurs). The vertical line ($g = 77$ μm) divides the excitation of the resonance modes into underdamped and overdamped regions [16]. Experimental results fit well with the CMT model. Fig. 10(b) shows the resonance frequency with respect to air gap according to Fig. 9(a) and (b). The resonance, which originates from the spoof SPPs resonance of the corrugated doped silicon, redshifts with the increase of air gap due to the change of effective propagation constant from perturbation of prism.

We also plotted the Smith chart according to the reflectivity and phase at a different frequency with air gap changing (see Fig. 11). when $g < 77$ μm, the Smith curve (red and black) passes through the four quadrants of the plane, indicating that the reflective phase varies from 0° to 360°. With the increase of the air gap, the trend of phase change decreases gradually. From the above analysis, it can be obviously seen that the state changes from the underdamped to overdamped with controlling the air gap.

Phase transition can further result in GH shift which can be written by the stationary-phase approach [33]

$$S = -\frac{c * \cos\theta}{2\pi\sqrt{\varepsilon}\sin\theta}\frac{d\varphi\left(\frac{B_2}{A_2}\right)}{df} \tag{19}$$

where *c* is the speed of light in vacuum. The THz wave lateral displacement that is normalized by wavelength ($\sim$385 μm) at 0.78 THz was calculated with different air gap as shown in Fig. 12. When the $g < 77$ μm, we can obtain a positive lateral displacement and when $g = 77$ μm, the THz wave lateral shift reaches the maximum. However, the negative shift occurs when

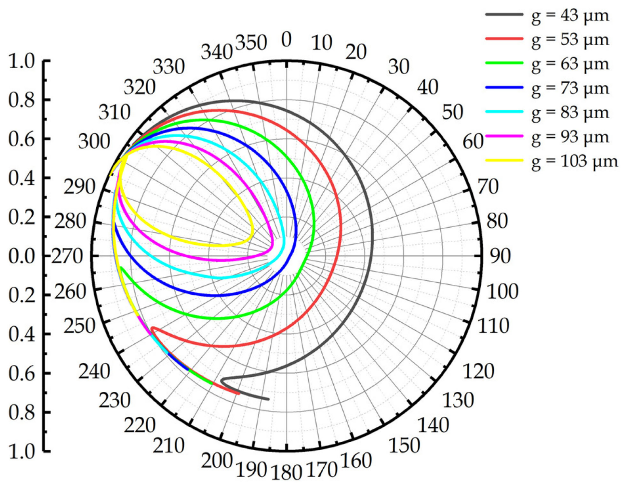

Fig. 11. Smith chart of reflectivity and phase with respect to different air gap value.

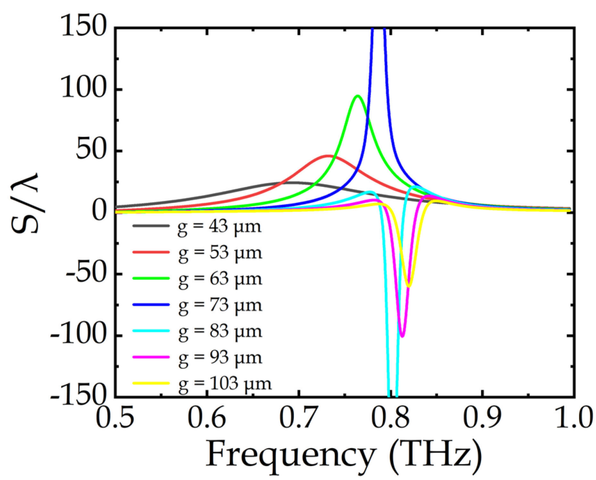

Fig. 12. Lateral wave displacement with different air gap.

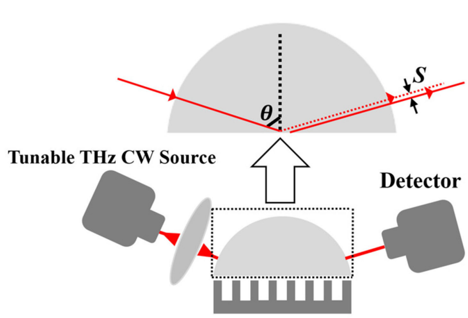

Fig. 13. Experimental scheme of GH shift.

$g > 77$ μm. As we explained previously, the lateral wave shift was depended on the radiative and intrinsic losses [44].

Next we discuss the possible experimental scheme of GH shift in prism coupled metasurface system. The experimental scheme is depicted in Fig. 13. The THz radiation with frequency f_1 from a tunable continuous-wave THz source is incident, through the center of the focusing lens. The reflected beam can be measured by detector which is moved along the interface to find the position of the peak of electric field. The reflective

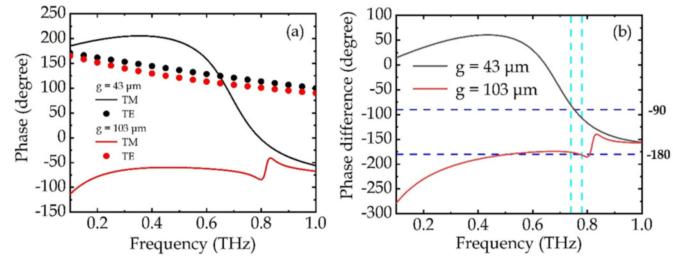

Fig. 14. Performance of the proposed polarization converter (a) Phases of reflection wave at $g = 43$ μm (black) and 103 μm (red) for TE (dot) and TM (line) polarization. (b) Their phase differences.

beam from prism without metasurface serves as a reference. The relative GH shift is the shift difference between reference and system. The related experiment will be performed in the future contribution. We believe that our present design will provide the guide useful for future measurement.

IV. Conclusion

In this article, phase transition has been found in an ATR configuration-based metasurface by narrowband tunability. A CMT was introduced to find the critical point by controlling the intrinsic and radiative losses. We demonstrated that the phase and amplitude of the reflected plane wave was closely related to radiative loss by tuning air gap. The results of the CMT model was verified by simulation and experimental results. Finally, we also demonstrated the positive and negative lateral THz wave displacement can be controlled by tuning the air gap which is dependent on the radiative loss. Since the air gap can be easily mechanically adjusted, the phase transition can be tunable and have been used in multifunctional devices with different phases switch. It should be noted that the phase transition could be further tailored by filling with lossy analytes, which can further tune the intrinsic (absorptive) loss [44]. We hope that our work can pave the wave for THz phase transition devices.

The phase transition with different air gap has enabled many applications in a diversified field. For instance, the phase diagram with different air gap can be used for designing multifunctional devices that can be actively switched between different phases. Here we take the application of polarization modulation for example. Fig. 14(a) shows the phase of reflected THz wave for TE and TM polarizations at $g = 43$ μm (underdamped state) and 103 μm (overdamped state). Their phase difference is approximately equal to -90° at $g = 43$ μm and -180° at $g = 103$ μm in a frequency range from 0.74 to 0.78 THz. It implies that the linearly-polarized incident wave is converted into the circularly-polarized wave at $g = 43$ μm, and the linearly-polarized incident wave is converted into the perpendicular linearly-polarized wave at $g = 103$ μm. By tuning the air gap, multifunctional polarization converter is made due to the large phase change from underdamped regime to overdampled regime in ATR based metasurface.

Moreover, the resonance frequency can be tuned to coincide with the fingerprint peak of the target sample to achieve absorption induced transparency [45], [46]. The ability to adjust the air gap during operation makes the fingerprint sensor quite robust to variations in the fabrication process. Since the air gap can also be electrically tuned by using mechanical stage controlled by piezo-electric actuator, these results will guide our application work, which we hope to complete in the future.

REFERENCES

[1] T. Nagatsuma *et al.*, "Advances in terahertz communications accelerated by photonics," *Nature Photon.*, vol. 10, pp. 371–379, 2016.

[2] K. Sengupta *et al.*, "Terahertz integrated electronic and hybrid electronic-photonic systems," *Nature Electron.*, vol. 1, pp. 622–635, 2018.

[3] D. M. Mittleman, "Perspective: Terahertz science and technology," *J. Appl. Phys.*, vol. 122, no. 23, 2017, Art. no. 230901.

[4] M. Rahm *et al.*, "THz wave modulators: A brief review on different modulation techniques," *J. Infrared, Millim., Terahertz Waves.*, vol. 34, no. 1, pp. 1–27, 2013.

[5] Y. Huang, S. C. Zhong, H. Z. Yao, and D. X. Cui, "Tunable terahertz plasmonic sensor based on graphene/insulator stacks," *IEEE Photon. J.*, vol. 9, no. 1, Feb. 2017, Art. no. 5900210.

[6] A. Arbabi *et al.*, "Dielectric metasurfaces for complete control of phase and polarization with subwavelength spatial resolution and high transmission," *Nature Nanotechnol.*, vol. 10, no. 11, pp. 937–943, 2015.

[7] L. Chen *et al.*, "Defect-induced fano resonances in corrugated plasmonic metamaterials," *Adv. Opt. Mater.*, vol. 5, no. 8, 2017, Art. no. 1600960.

[8] L. Chen *et al.*, "Controllable multiband terahertz notch filter based on a parallel plate waveguide with a single deep groove," *Opt. Lett.*, vol. 39, no. 15, pp. 4541–4544, 2014.

[9] F. Hu *et al.*, "Intensity modulation of a terahertz bandpass filter: utilizing image currents induced on MEMS reconfigurable metamaterials," *Opt. Lett.*, vol. 43, no. 1, pp. 17–20, 2018.

[10] X. Liu *et al.*, "Experimental realization of a terahertz all-dielectric metasurface absorber," *Opt. Express*, vol. 25, no. 1, pp. 191–201, 2017.

[11] W. S. L. Lee *et al.*, "Broadband terahertz circular-polarization beam splitter," *Adv. Opt. Mater.*, vol. 6, no. 3, 2018, Art. no. 1700852.

[12] X. Zang *et al.*, "Manipulating terahertz plasmonic vortex based on geometric and dynamic phase," *Adv. Opt. Mater.*, vol. 7, no. 3, 2019, Art. no. 1801328.

[13] L. Cong *et al.*, "All-optical active THz metasurfaces for ultrafast polarization switching and dynamic beam splitting," *Light, Sci. Appl.*, vol. 7, 2018, Art. no. 28.

[14] C. Sheng *et al.*, "Definite photon deflections of topological defects in metasurfaces and symmetry-breaking phase transitions with material loss," *Nature Commun.*, vol. 9, 2018, Art. no. 4271.

[15] B. You *et al.*, "Terahertz artificial material based on integrated metal-rod-array for phase sensitive fluid detection," *Opt. Express*, vol. 25, no. 8, pp. 8571–8583, 2017.

[16] L. Cong *et al.*, "Active phase transition via loss engineering in a terahertz MEMS metamaterial," *Adv. Mater.*, vol. 29, no. 26, 2017, Art. no. 1700733.

[17] M. Navarro-Cia *et al.*, "Negative group delay through subwavelength hole arrays," *Phys. Rev. B*, vol. 84, no. 7, 2011, Art. no. 075151.

[18] Y. Qing *et al.*, "Tailoring anisotropic perfect absorption in monolayer black phosphorus by critical coupling at terahertz frequencies," *Opt. Express*, vol. 26, no. 25, pp. 32442–32450, 2018.

[19] Z. Miao *et al.*, "Widely tunable terahertz phase modulation with gate-controlled graphene metasurfaces," *Phys. Rev. X.*, vol. 5, no. 4, 2015, Art. no. 041027.

[20] C. Qu *et al.*, "Tailor the functionalities of metasurfaces based on a complete phase diagram," *Phys. Rev. Lett.*, vol. 5, no. 4, 2015, Art. no. 235503.

[21] T.-T. Kim *et al.*, "Electrical access to critical coupling of circularly polarized waves in graphene chiral metamaterials," *Sci. Adv.*, vol. 3, no. 9, 2017, Art. no. 701377.

[22] Z. Chen *et al.*, "Graphene controlled brewster angle device for ultra-broadband terahertz modulation," *Nat. Commun.*, vol. 9, no. 1, 2018, Art. no. 4909.

[23] X. Liu *et al.*, "Graphene based terahertz light modulator in total internal reflection geometry," *Adv. Opt. Mater.*, vol. 5, no. 3, 2017, Art. no. 1600697.

[24] J. F. O. Hara *et al.*, "Prism coupling to terahertz surface plasmon polaritons," *Opt. Express*, vol. 13, no. 16, pp. 6117–6126, 2005.

[25] B. Ng *et al.*, "Spoof plasmon surfaces: A novel platform for THz sensing," *Adv. Opt. Mater.*, vol. 1, no. 8, pp. 543–548, 2013.

[26] M. J. Ehrlich and L. L. Newkirk, "Corrugated surface antennas," in *Proc. IRE Int. Convention Rec.*, 1958, pp. 18–33.

[27] A. A. Oliner and A. Hessel, "Guided waves on sinusoidally-modulatd reactance surface," *IRE Trans. Antennas Propag.*, vol. 7, no. S201, pp. 161–165, 1959.

[28] A. F. Harvey, "Periodic and guiding structures at microwave frequencies," *IRE Trans. Microw. Theory Techn.*, vol. 8, pp. 30–61, 1960.

[29] R Ulrich and M Tacke, "Submillimeter waveguiding on periodic metal structure," *Appl. Phys. Lett.*, vol. 22, pp. 251–253, 1973.

[30] J. B. Pendry *et al.*, "Mimicking surface plasmons with structured surfaces," *Science*, vol. 305, no. 5685, pp. 847–848, 2004.

[31] L. Chen *et al.*, "Excitation of dark multipolar plasmonic resonances at terahertz frequencies," *Sci. Rep.*, vol. 6, 2016, Art. no. 22027.

[32] L. Chen *et al.*, "Mode splitting transmission effect of surface wave excitation through a metal hole array," *Light, Sci. Appl.*, vol. 2, no. 3, 2013.

[33] L. Chen *et al.*, "Observation of large positive and negative lateral shifts of a reflected beam from symmetrical metal-cladding waveguides," *Opt. Lett.*, vol. 32, no. 11, pp. 1432–1434, 2007.

[34] S. Ramani, M. T. Reiten, P. L. Colestock, A. J. Taylor, A. K. Azad, and J. F. O'Hara, "Electromagnetic response of finite terahertz metafilm arrays excited on total internal reflection boundaries," *IEEE Trans. THz Sci. Technol.*, vol. 3, no. 6, pp. 709–720, Nov. 2013.

[35] H. Yao and S. Zhong, "High-mode spoof SPP of periodic metal grooves for ultra-sensitive terahertz sensing," *Opt. Express*, vol. 22, no. 21, pp. 25149–25160, 2014.

[36] R. Ulrich, "Theory of the prism–film coupler by plane-wave analysis," *J. Opt. Soc. Am.*, vol. 60, no. 10, pp. 1337–1350, 1970.

[37] R. Ulrich and R. Torge, "Measurement of thin film parameters with a prism coupler," *Appl. Opt.*, vol. 12, no. 12, pp. 2901–2908, 1973.

[38] L. Chen *et al.*, "Ultra-sensitive fluid fill height sensing based on spoof surface plasmon polaritons," *J. Electromagn. Waves Appl.*, vol. 32, no. 4, pp. 471–482, 2018.

[39] M. M. Nazarov, A. P. Shkurinov, F. Garet, and J.-L. Coutaz, "Characterization of highly doped si through the excitation of THz surface plasmons," *IEEE Trans. THz Sci. Technol.*, vol. 5, no. 4, pp. 680–686, Jul. 2015.

[40] G. Kumar, S. Li, M. M. Jadidi, and T. E. Murphy, "Terahertz surface plasmon waveguide based on a one-dimensional array of silicon pillars," *New J. Phys.*, vol. 15, no. 8, 2013, Art. no. 085031.

[41] M. Born and E. Wolf, *Principles of Optics*, 7th ed. Cambridge, U.K.: Cambridge Univ. Press, 1999.

[42] E. Hendry *et al.*, "Importance of diffraction in determining the dispersion of designer surface plasmons," *Phys. Rev. B*, vol. 78, 2008, Art. no. 235426.

[43] L. Chen *et al.*, "Observation of electromagnetically induced transparency-like transmission in terahertz asymmetric waveguide-cavities systems," *Opt. Lett.*, vol. 38, no. 9, pp. 1379–1381, 2013.

[44] L. Chen *et al.*, "Mechanism of giant goos−Hänchen effect enhanced by long-range surface plasmon excitation," *J. Opt.*, vol. 13, no. 3, 2011, Art. no. 035002.

[45] L. Chen *et al.*, "Terahertz time-domain spectroscopy and micro-cavity components for probing samples: A review," *Front. Inf. Technol. Electron. Eng.*, vol. 20, no. 5, pp. 591–607, 2019.

[46] R. Adato, A. Artar, S. Erramilli, and H. Altug, "Engineered absorption enhancement and induced transparency in coupled molecular and plasmonic resonator systems," *Nano Lett.*, vol. 13, no. 6, pp. 2584–2591, 2013.

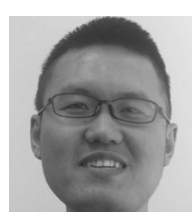

Lin Chen (M'19) received the B.S. and M.S. degrees in electrical engineering from Southeast University, Jiangsu, China, in 2002 and 2005, respectively, and the Ph.D. degree in optics from Shanghai Jiao Tong University, Shanghai, China, in 2008.

Since 2008, he has been with the College of Optical-Electrical and Computer Engineering, University of Shanghai for Science and Technology, Shanghai, China, where he is currently the Faculty of communication engineering. From 2007 to 2008, he was with Avanex Corporation as Senior Engineer. From 2012 to 2013, he was a Visiting Scholar with the State Key Laboratory of Millimeter Waves (meta-group of Tie Jun Cui), Southeast University. From 2015 to 2016, he was a Visiting Researcher with Ultrafast THz Optoelectronic Laboratory, Oklahoma State University, Stillwater, OK, USA. He has authored or coauthored more than 60 Science Citation Indexed peer reviewed papers (include 3 Highly Cited Papers) and 18 patents. One paper was selected as best of Advanced Optical Materials in 2017. His research interests include terahertz waveguides, metamaterials, and labs on chips.

Dr. Chen had been designated "Shu Guang" Scholar, Shanghai Top-Notch Young Talents in 2018, and 2018 Publons peer review reward.

Yifan Ge was born in Jiangsu, China, in 1994. He received the B.S. degree in information engineering from the Xu Hai College of China, University of Mining and Technology, XuZhou, China, in 2017. He is currently working toward the M.S. degree in information engineering at the University of Shanghai for Science and Technology, Shanghai, China.

His research interests include terahertz waveguides, broadband filters, and sensor chips.

Xiaofei Zang received the B.S. degree in physics from Jiangsu Normal University, Jiangsu, China, in 2005, and the Ph.D. degree in electronic and communication engineering from Shanghai Jiaotong University, Shanghai, China, in 2012.

He has authored or coauthored more than 30 scientific papers in refereed journals. His research interests include concentrated in the areas of terahertz (THz) functional device and transformation optics. Specific research topics include THz absorber, THz isolator, cloak, high-directional antenna, and super-resolution imaging.

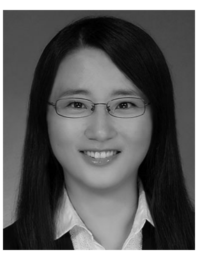

Jingya Xie received the Ph.D. degree in electronic engineering from Shanghai Jiao Tong University, Shanghai, China, in 2015.

She entered the College of Optical-Electrical and Computer Engineering, University of Shanghai for Science and Technology, Shanghai, China, engaged in integrated optoelectronic devices and its application research in terahertz communication systems.

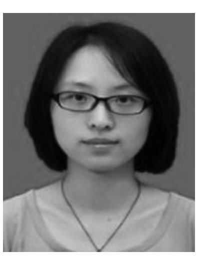

Li Ding received the bachelor's and master's degrees from the University of Electronic Science and Technology of China, Chengdu, China, in 2008, and the Ph.D. degree from the University of Science and Technology of China, Hefei, China, in 2011, all in electronic engineering.

She is currently an Assistant Professor with the University of Shanghai for Science and Technology, Shanghai, China. Her research interests include millimeter-wave and terahertz-wave technology, especially with the applications to target detection and imaging.

Alexei V. Balakin received the M.S. degree in physics and Ph.D. degree in physical and mathematical science (with a specialty in laser physics) from Lomonosov Moscow State University, Moscow, Russia, in 1995 and 1998, respectively.

Since 1998, he has been a member of the Physics Faculty of Lomonosov Moscow State University. He is currently a Senior Researcher. He has authored and coauthored more than 70 articles and theses. His research interests include laser physics and nonlinear optics in general and generation and application of terahertz pulsed radiation currently.

Alexander P. Shkurinov received the Ph.D. degree and the Doctor of Physics and Math Sciences (Habilitation) degree from M.V. Lomonosov Moscow State University, Moscow, Russia, in 1988 and 2013, respectively.

Since 2015, he has been a Professor with the Faculty of Physics of MSU. He has authored and coauthored more than 300 papers in peer-reviewed scientific journals, was invited to deliver more than 60 invited lectures and talks. His research interests include the development and application of femtosecond laser techniques, time-resolved spectroscopy of molecules in liquid phase, nonlinear optics and THz techniques and spectroscopy.

Dr. Shkurinov was the recipient of the Medal in the honor of Prof. Rozhdestvensky for his contribution into the development of optical science and technology by the Russian Optical Society in 2008.

Yiming Zhu received the B.S. and M.S. degrees in applied physics from Shanghai Jiaotong University, Shanghai, China, in 2002 and 2004, respectively, and the Ph.D. degree in electronics engineering from the University of Tokyo, Tokyo, Japan, in 2008.

He is currently a Professor with the University of Shanghai for Science and Technology, Shanghai, China, and the Vice Director of the Shanghai Key Lab of Modern Optical System. He has authored or coauthored more than 70 papers on SCI journals.

Prof. Zhu was the recipient of the Japanese Government (Monbukagakusho) Scholarship in 2004.